

The Roles of Vertical Advection and Eddy Diffusion in the Equatorial Mesospheric Semi-annual Oscillation (MSAO)

R.L. Gattinger¹, E. Kyrölä², C.D. Boone³, W.F.J. Evans^{4,5},
K.A. Walker^{6,3}, I.C. McDade⁷,
P.F. Bernath^{8,3} and E.J. Llewellyn¹

¹ISAS, Department of Physics and Engineering Physics, 116 Science Place, University of Saskatchewan, Saskatoon SK, S7N 5E2, Canada

²Finnish Meteorological Institute, Earth Observation, P.O. Box 503, FI-00101, Helsinki, Finland

³Department of Chemistry, University of Waterloo, Waterloo, ON, N2L 3G1, Canada

⁴NorthWest Research Associates Inc., 4118 148 Avenue N.E., Redmond WA 98052, USA

⁵Centre for Research in Earth and Space Science (CRESS), York University, 4700 Keele Street, Toronto, ON, M3J 1P3, Canada

⁶Department of Physics, University of Toronto, 60 St. George Street, Toronto, ON, M5S 1A7, Canada

⁷Department of Earth and Space Science and Engineering (ESSE), York University, 4700 Keele Street, Toronto, ON, M3J 1P3, Canada

⁸Department of Chemistry and Biochemistry, Old Dominion University, 4541 Hampton Boulevard, Norfolk, Virginia 23529-0126

Abstract

Observations of the mesospheric semi-annual oscillation (MSAO) in the equatorial region have been reported dating back several decades. Seasonal variations in both species densities and airglow emissions are well documented. The extensive observations available offer an excellent case study for comparison with model simulations. A broad range of MSAO measurements is summarised with emphasis on the 80 to 100 km region. The objective here is not to address directly the complicated driving forces of the MSAO, but rather to employ a combination of observations and model simulations to estimate the limits of some of the underlying dynamical processes. Photochemical model simulations are included for near-equinox and near-solstice conditions, the two times with notable differences in the observed MSAO parameters. Diurnal tides are incorporated in the model to facilitate comparisons of observations made at different local times. The roles of water vapour as the 'driver' species and ozone as the 'response' species are examined to test for consistency between the model results and observations. The simulations suggest the interactions between eddy diffusion and background vertical advection play a significant role in the MSAO phenomenon. Further, the simulations imply there are rigid limits on vertical advection rates and eddy diffusion rates. For August at the equator, 90 km altitude, the derived eddy diffusion rate is approximately $1 \times 10^6 \text{ cm}^2 \text{ s}^{-1}$ and the vertical advection is upwards at 0.8 cm s^{-1} . For April the corresponding values are $4 \times 10^5 \text{ cm}^2 \text{ s}^{-1}$ and 0.1 cm s^{-1} . These results from the current 1D model simulations will need to be verified by a full 3D simulation. Exactly how vertical advection and eddy diffusion are related to gravity wave momentum as discussed by Dunkerton [1982] three decades ago remains to be addressed.

Introduction

Observations of the mesospheric semi-annual oscillation (MSAO) in equatorial airglow emissions have been documented dating back several decades, for example the ground-based data of Fukuyama [1977] who observed seasonal variations in OI 5577Å (OI), in the hydroxyl (OH*) and sodium (Na*) airglow emissions at low latitude stations. Cogger *et al.* [1981] observed a pronounced seasonal variation in the ISIS OI airglow data. Burrage *et al.* [1994] found a persistent seasonal variation in the O₂ atmospheric A band (O₂ A) using the UARS/HRDI instrument, the brightness being well correlated with the horizontal meridional wind field. A more recent example is that of Shepherd *et al.* [2006] using data from the UARS/WINDII instrument covering the period from 1992 through 1995. They found a recurring seasonal variation in night-time OI centred on 96 km and in OH* centred on 87 km, the maxima being at the equinox periods. Observations by Skinner *et al.* [1998], also using the UARS HRDI instrument, found very similar results.

The equatorial MSAO can also be seen in measurements of minor species in the 90 km altitude region. Thomas [1995] presented atomic hydrogen (H) and atomic oxygen (O) climatologies which clearly showed the MSAO. Chandra *et al.* [1997] observed seasonal variations in water vapour (H₂O) using UARS/MLS and HALOE data and in addition obtained good agreement with a two-dimensional (2D) photochemical and transport model. Lossow *et al.* [2008] using the SMR data from the Odin spacecraft [Murtagh *et al.*, 2002] observed the MSAO in H₂O mixing ratio, at 90 km the maxima occurred in the solstice periods. Kyrölä *et al.* [2006, 2010] using Envisat/GOMOS data found that ozone (O₃) at 90 km peaked in equinox periods and was approximately a factor of three lower in solstice periods. Huang *et al.* [2008] and Smith *et al.* [2008] found a similar variation in O₃ using data from the TIMED/SABER instrument. Seasonal oscillations in mesospheric atomic oxygen (O) were inferred by Sheese *et al.* [2011] using observations from the OSIRIS instrument [Llewellyn *et al.*, 2004] on Odin, and by Smith *et al.* [2010] using TIMED SABER data. Both of these O studies also showed diurnal variations. The semi-annual oscillation at higher latitudes, not the focus of the current study, transitions into an annual oscillation [Thomas, 1990; Kyrölä *et al.*, 2010].

Numerous model simulations of the MSAO driving forces have been published. Dunkerton [1982] originally suggested that the MSAO was driven from below by gravity wave momentum. Easterly and westerly phase speed waves are selectively transmitted through the semi-annually varying stratopause wind phases. Richter and Garcia [2006] evaluated the relative importance of the various MSAO forcing terms included in the WACCM2 model and concluded that at solstice the mechanism proposed by Dunkerton is the dominant source of the strong mesospheric westerlies, but there are opposing

easterlies driven by meridional advection. However, they found that at equinox the MSAO easterlies are not satisfactorily simulated by the WACCM2 model. Richter *et al.* [2008], using WACCM3, addressed the complex interaction between gravity waves and horizontal winds and again pointed out the model limitations. Alexander *et al.* [2010] provided an extensive review of gravity wave observations and associated model parameterisations and discussed the agreements, and disparities, between model predictions and observations. In summary, differences between model simulations and MSAO observations are not yet adequately explained.

The following sections contain comparisons between simulations using a time-dependent one-dimensional (1D) photochemical model and observations from various sources. Diurnal tides, eddy diffusion and the prevailing background vertical winds make up the dynamic components included in the 1D model. More detailed examples of such combined photochemical and dynamical model comparisons with observations are those of Marsh *et al.* [2003], Smith and Marsh [2005] based on the ROSE model, Wu *et al.* [2008] with the TIME-GCM model, and Dikty *et al.* [2010] using the HAMMONIA model. The focus here is intentionally limited to addressing the observed MSAO in the equatorial region. The present objective is not to address directly the complicated driving forces of the MSAO but rather to employ a combination of observations and model simulations to estimate the limits of the some of the dynamical processes.

The diurnal tides [Hagan *et al.*, 1999] are necessarily included in the model since they have a significant impact on instantaneous measurements of minor species densities and airglow emissions [Smith, 2004], particularly in the equatorial mesosphere. Yee *et al.* [1997] demonstrated the effects of diurnal tides in their extensive model simulations of the UARS/HRDI observations. Smith *et al.* [2010] have also successfully simulated the significant diurnal tidal effects in the O observations made with SABER. Studies by Wu *et al.* [2008] and John and Kumar [2011] provide further insight into the details of the tides. When comparing observations made at different local times the tidal effect must be considered. Conversely, observations of selected species made at differing local times can be used to validate model simulations of the tides.

Similarly, eddy diffusion has a significant impact on the vertical distribution of mesospheric minor species. Instances of such studies are those of Vlasov and Kelley [2010] for the effects of turbulence on the O vertical profile, and similarly by Sonnemann and Körner [2003] for the H profile. The seasonal variation of eddy diffusion at low latitude, the target latitude for the current study, was derived from MST radar observations by Sasi and Vijayan [2001] with maximum turbulence observed at solstice periods. Seasonal variations of eddy diffusion have also been inferred by Liu [2009] for

mid-latitudes and by Hall *et al.* [1999] at high latitudes, which potentially provide realistic constraints for future studies.

For the MSAO comparisons the following sections include two simulation periods, one simulation for near equinox conditions and one for near solstice conditions. The seasonal dependencies noted in the observations summarised above are discussed in more detail and are used as ‘constraints’ in the model simulations of diurnal minor species density variations and related airglow emissions. In particular, since O_3 is a short-lived species at 90 km, relative to O and H, and since O_3 densities are driven by O and H, and temperature, O_3 is consequently used as a probe for the longer-lived O and H species. How this leads to the determination of the dynamical variations in the equatorial MSAO is discussed in the following sections.

MSAO Data Driving the Model Simulation

A strong equatorial MSAO was observed in the H_2O mixing ratio by Lossow *et al.* [2008] with the 90 km mixing ratio varying from approximately 0.1 ppm in April to approximately 0.4 ppm in July. The upper altitude limit of their published profiles is 100 km. A similar equatorial seasonal variation is observed in H_2O profiles measured with the MLS instrument on the Aura spacecraft [McCormack *et al.*, 2008]. At solstice the Aura group recommended an H_2O mixing ratio at 90 km of approximately 1 ppm, the upper altitude of approximately 90 km being limited by the MLS observations. In the current study the equatorial MSAO in H_2O is taken from the ACE-FTS instrument on SCISAT [Bernath *et al.*, 2005], again increasing from approximately 0.1 ppm at 90 km in April to approximately 0.6 ppm in August. For the model initial conditions the ACE-FTS H_2O profiles from approximately 15° North to 15° South are averaged over approximately 5 days, that is, the time it takes for the ACE-FTS observations to traverse that latitude range.

Since the simulation here is based on a 1D model, the effects of latitudinal gradients are not included. For the range from 15° South to 30° South the average ACE-FTS H_2O mixing ratio for April, at 90 km altitude, is approximately 0.1 ppm, the same as in the region spanning the equator. For 15° North to 30° North the average is approximately 0.13 ppm. These measured changes with latitude do not significantly affect the final conclusions.

The H profiles assumed in the model initial conditions were determined using data from Thomas [1990, 1995] who constructed a seasonal and latitudinal climatology for H, as well as for O, from the Solar Mesosphere Explorer (SME) observations. The SME equatorial H densities near the mesopause

at solstice were approximately twice as large as at equinox. For similar conditions Xu *et al.* [2012] inferred an H seasonal variation of a factor of three using the SABER dataset. Sharp and Kita [1987] made a direct measurement of the H profile, but at mid-latitudes, thus not as relevant for the present purposes. Ultimately, the model simulation of H is derived from the measured H₂O profile combined with the solar photo-dissociation by Lyman α with the input solar flux obtained from the LASP Solar Irradiance Data Center. Relating to mesospheric odd H species, Shapiro *et al.* [2012] documented the direct connection between ground state hydroxyl (OH) and H₂O densities and the Lyman α variation with the 27-day solar rotation cycle.

Seasonal variations of vertical profiles of O [Sheese *et al.*, 2011] are included in the model analysis as initial conditions with data from the OSIRIS instrument on Odin. The O densities are derived from observed O₂ A-band vertical profiles following the method of McDade *et al.* [1986]. The derived seasonal variations are similar to those observed by Thomas [1995] and by Xu *et al.* [2012].

The background atmosphere assumed in the simulation is based on the ACE-FTS measurements of temperature and density which are in general agreement with the NRL-MSISE-00 model estimates by Picone *et al.* [2002]. Initial conditions for near equinox and near solstice simulations are selected from the ACE-FTS data where both sunrise and sunset observations at low latitude occur within approximately a ten day period, these periods are determined by the ACE-FTS orbital parameters as occurring in mid-April and in mid-August. In the current work only these two specific cases are considered since they occur at times near the maxima and the minima of the H₂O and O₃ MSAO.

The seasonal variation of eddy diffusion at low latitudes, the target latitude for the current study, was obtained from the MST radar results by Sasi and Vijayan [2001]. They observed a maximum in turbulence at solstice with an eddy diffusion rate of approximately $2 \times 10^6 \text{ cm}^2 \text{ s}^{-1}$ at 90 km altitude and a minimum of approximately $3 \times 10^5 \text{ cm}^2 \text{ s}^{-1}$ at equinox. Qian *et al.* [2009] adopted a very similar eddy diffusion pattern for the lower boundary of their TIE-GCM simulation of the seasonal variation of the thermosphere. The baseline eddy diffusion rates adopted here are $4 \times 10^5 \text{ cm}^2 \text{ s}^{-1}$ for April and $1 \times 10^6 \text{ cm}^2 \text{ s}^{-1}$ for August.

The impact of vertical advection on species profiles is also included in the model. Beginning with an extensive horizontal wind model based on comprehensive observations Portnyagin *et al.* [2010] derived seasonal vertical wind profiles as a function of latitude. The analysis was based on monthly means of zonally averaged meridional winds. For April in the equatorial region they inferred a prevailing downward wind of approximately 0.5 cm s^{-1} at 90 km altitude and for July a similar but upward wind. Unfortunately, their estimated errors for the derived vertical winds were of comparable

magnitude. Richter and Garcia [2006, their Figure 5], using WACCM2, inferred the equatorial upward advection for August to be larger than for April. Fauliot *et al.* [1997] derived equatorial prevailing vertical winds using UARS/WINDII data, the inferred values being in the range of 1 cm s^{-1} . Chandra *et al.* [1997] found from their 2D model that the 77 km altitude prevailing vertical winds at 45° North varied from approximately null in April to 0.5 cm s^{-1} upwards in August. The equatorial diurnal tides contain an oscillating vertical component, in contrast to the prevailing vertical wind. According to Hagan *et al.* [1999] the tidal vertical wind amplitude for April is approximately 20% larger than for August.

Starting with the various initial conditions listed above, diurnal simulations were conducted for the April near-equinox conditions and for August. The details of the model photochemistry and dynamics are briefly described below. Simulations were conducted over a period of ten model days to check for approximate convergence to a diurnally repeating steady state. Diurnal variations of the altitude profiles for a number of species for model days seven and eight are presented. Interactions between photochemical effects and dynamical effects, including molecular diffusion, eddy diffusion and diurnal migrating tides, are explored.

Simulations of the Relevant Species Profiles

As mentioned above the simulations are performed with a time-dependent 1D model including photochemical and dynamical components tailored to the mesosphere and lower thermosphere. Time varying solutions are obtained for O, O₃, O₂(¹Δ), H, molecular hydrogen (H₂), H₂O, OH, perhydroxyl (HO₂), hydrogen peroxide (H₂O₂), carbon monoxide (CO) and carbon dioxide (CO₂). The underlying photochemical continuity equations are described in detail by Brasseur and Solomon [2005]. Adopted reaction rates follow those given by Sander *et al.* [2011]. Solar flux and photolysis cross sections cover the 116 nm to 725 nm spectral range. For water vapour and molecular oxygen particular attention is paid to the important roles played by solar radiation at Lyman-α [Lewis *et al.*, 1983; Chabrillat and Kockarts, 1997] and in the Schumann-Runge bands [Kockarts, 1994]. Lyman-α flux values are obtained from the SORCE compilations. Diurnally varying photolysis rates are recalculated at 1° solar elevation angle increments and at 1 km intervals throughout the model range. The numerical integration algorithms are designed to deal with the wide range of time constants exhibited by the mesospheric chemical reactions, from the fast catalytic recycling of OH_x in the removal of odd oxygen to the slow rate of odd hydrogen removal near the mesopause.

The continuity equations describing eddy diffusion and molecular diffusion are also provided by Brasseur and Solomon [2005]. A tri-diagonal matrix formulation covering the altitude range is solved for the longer lived species, namely O, H, H₂, H₂O, CO and CO₂. The thermospheric model results of Tian *et al.* [2008] are used as a check on the simulated H densities at the model upper boundary, in the 110 km range.

For the numerical simulation of vertical winds and diurnal tides the nonlinear nature of atmospheric vertical distribution poses a problem. Holton [2004] and Brasseur and Solomon [2005] listed mathematical techniques which have been used, with partial success, to introduce vertical advection. Building on previous approaches, non-linear fitting methods for each species are employed in the current model to simulate vertical transport across layer intersections. Tests over periods longer than the 10 day simulation reported here were conducted to ensure residual numerical error propagation was less than a few percent. For the 1D model the diurnal tidal phases and amplitudes for April and for August are from Hagan *et al.* [1999]. The tides are included as both temperature oscillations and vertical winds.

From the simulations presented here that are intended to provide agreement with the MSAO observations described above, the baseline 90 km vertical eddy diffusion rates employed in the model are $4 \times 10^5 \text{ cm}^2 \text{ s}^{-1}$ and $1 \times 10^6 \text{ cm}^2 \text{ s}^{-1}$ for April and August respectively. The baseline background vertical advection in the 90 km region is upwards at 0.1 cm s^{-1} for April and 0.8 cm s^{-1} for August. This combined effect of eddy diffusion and vertical advection on the measured species profiles is investigated further in a later section.

Since H₂O is one of the major drivers in upper mesospheric photochemistry via the catalytic role of odd H, the discussion of the MSAO begins here with model simulations of H₂O profiles for April near equinox conditions (Figure 1a) and August near solstice conditions (Figure 1b). Note the change in scale between Figure 1a and Figure 1b, and likewise for subsequent figure pairs. The steep drop in the April mixing ratio from 80 km to 90 km is very pronounced, much more than for the August profile. For the model H₂O initial conditions the average of sunrise and sunset ACE-FTS profiles is assumed. This is commensurate with numerical integration beginning at local noon in the model. A difference between ACE-FTS sunrise and sunset H₂O profiles is apparent, a clear manifestation of the diurnal tidal effect. Time-dependent solutions for the H₂O profiles include all dynamical terms and relevant photochemical reactions. Evidence of the diurnal tide is clearly present in both Figures 1a and 1b.

From these H₂O profiles come the model H profiles shown in Figure 2a for April and Figure 2b for August. The April H densities are approximately two-thirds the August values over most of the

altitude region. From 88 to 100 km the H mixing ratio is approximately constant, in agreement with model calculations by Sonnemann and Körner [2003], so reducing the signature of the diurnal tide. Around 85 km, where the H mixing ratio does change with altitude, the H density exhibits a diurnal tidal effect with maximum H values occurring several hours after ground-level sunset. Below 80 km the H density is driven primarily by photochemistry with the density increasing in the afternoon hours, thus replacing the loss of odd H species that occurred during the previous night.

The model O profiles for April are shown in Figure 3a and for August in Figure 3b. The maximum O densities for August are approximately one-half those for April. The diurnal tides are again apparent. Above 100 km the effects of the semi-diurnal tides, also included in the 1D model simulation, are readily seen.

Model O₃ profiles for April are shown in Figure 4a and for August in Figure 4b. Again the diurnal tides are obviously present, but are more complex than for O as a result of the strong temperature dependence of the O/O₃ partitioning. The temperature minimum, which occurs near 05 Local Time (LT), results in an increase in the O₃ density relative to O. The maximum model O₃ densities for August are less than one-half those for April.

The results for H₂O, H, O and O₃, in Figures 1 through 4 are compared in a later section with the MSAO observations. However, since the comparisons with observations are tied to the specific local times of the observations from multiple satellites the diurnal tides are discussed first. The impact of the diurnal tides can be significant, especially in the upper mesosphere and lower thermosphere. In addition the phase of the tides is altitude dependent, further complicating the comparisons involving multiple species.

Checking the Model Diurnal Tides

The diurnal variation of O shown in Figure 3a for April conditions and in Figure 3b for August conditions provides an opportunity to check the validity of the simulated tides. The local time phases of the model O tides as a function of altitude can be compared with the diurnal variations described by Smith *et al.* [2010] for O derived from the SABER observations. Beginning at 82 km, for equatorial vernal equinox, the O maximum from SABER data occurs between 23LT and 02 LT (their Figure 3) while for the current model it occurs between 21LT and 01LT (Figure 3a). Switching to the O minimum SABER results show that it is at 94 km between 00LT and 04LT (their Figure 4) while from Figure 3a the minimum is at 94 km is between 00LT and 03LT. Similarly, the equatorial O tides derived from the UARS/WINDII observations by Russell *et al.* [2005] show a maximum at 82 km

between 20LT and 01LT (their Figure 8) and a minimum at 94 km between 00LT and 05LT (their Figure 8). The agreement between the three sources is within 2 hours of local time.

The effects of diurnal tides are also clearly seen in the ACE-FTS sunrise versus sunset profiles for H₂O and for CO (Figure 5a). These species show a marked change in mixing ratio with altitude in the upper mesosphere and are consequently sensitive to the altitude shift caused by diurnal tides. Hence, these observed diurnal changes afford a further opportunity to validate the simulation of the diurnal tides. The model H₂O tides in Figure 1a are out of phase with the model CO tides in Figure 5b. This is expected since in the 90 km region the H₂O mixing ratio decreases with increasing altitude while the CO mixing ratio increases with altitude. The phases of the model tides in Figures 1a and 5b are in approximate agreement with those of Figure 5a. With the phases of the model tides appearing to be valid, comparisons using local time dependent observations of the MSAO are discussed in the next section.

MSAO – Model versus Observations

A persistent MSAO was observed in the night-time O₃ density by Kyrölä *et al.* [2010] using the GOMOS instrument on the Envisat satellite. The multi-year observations, extending from 2002 through 2008, exhibit a dominant semi-annual component at 90 km at the equator (Figure 6). The maximum O₃ densities, about $6 \times 10^8 \text{ cm}^{-3}$, occur just after equinox periods while the minima, about $2 \times 10^8 \text{ cm}^{-3}$, occur just after the solstice periods. The night-time measurements are between 21 LT and 24 LT, determined by the Envisat constant local time orbit. The individual O₃ density profiles extend up to approximately 100 km and clearly show the secondary peak near 90 km. The quasi-biennial oscillations noted by Shepherd *et al.* [2006] are not immediately apparent in the GOMOS O₃ observations in the equatorial region. Huang *et al.* [2008], using the SABER instrument on the TIMED satellite, also observed a strong seasonal variation in O₃ at 90 km at the equator. However, their maximum O₃ viewing altitude is limited to approximately 90 km and thus they do not delineate a secondary O₃ density peak as definitively.

Ozone densities from the model simulations for April and for August are shown as the large squares in Figure 6. These simulated densities are for the baseline eddy diffusion rates and background vertical advection indicated in the previous section.

A further comparison is included here, this one between model OH* and OSIRIS spectral observations of the MSAO for the OH* 9-4 Meinel emission band. Model volume emission rate (VER) profiles of

OH* 9-4 band total are shown for April in Figure 7a and for August in Figure 7b. The OH* product is determined from the model H and O₃ profiles. The OH* (v'=9) nascent band fractional production (0.47) and the deactivation rates for O₂, N₂ and O are from Adler-Golden [1997]. OH* rotational line transition probabilities are from the tabulations by van der Loo and Groenenboom [2007, 2008]. The seasonal variation of OH* 9-4 obtained from OSIRIS spectra observations is shown in Figure 8. Limb observations were converted to volume emission rate vertical profiles and then summed vertically to provide a reference to zenith observations. From the tabulations of Cosby and Slanger [2007] the observed OH* 9-4 brightness varies from approximately 300 to 900 Rayleighs (1R=10⁶ photons cm⁻² s⁻¹), without regard for time and location. The two large square symbols in Figure 8 indicate the model emission for April and for August at approximately 20 LT that correspond to the OSIRIS low latitude observations. Both model and observation show a decreased OH* from April to August although the ratios are different. Slightly better agreement is achieved by arbitrarily increasing the rate of removal of OH* (v'=9) by O by a factor of three (diamond symbols). As noted by Adler-Golden [1997] this rate is very uncertain. However, Smith *et al.* [2010] have concluded that the collision rate with O must be reduced to satisfy the SABER O density measurements.

Some portion of the equatorial MSAO can arise from the seasonal variation of solar insolation. Model calculations indicate that in the 85 to 95 km region the April to August change in the photodissociation rate of O₂ averaged over 24H is less than 5%. Similarly, seasonal changes in temperature can influence the O to O₃ ratio, and so impact the comparison here with the GOMOS O₃ observations. Model simulations for the local time of the GOMOS observations, approximately 23H, yield an April to August change of less than 5% in the 85 to 95 km region.

Interactions between Vertical Eddy Diffusion and Vertical Advection

The model results presented above, using August as an example, are for the baseline eddy diffusion rates of 1x10⁶ cm² s⁻¹ at 90 km altitude and for a vertical advection of 0.8 cm s⁻¹. The impact of arbitrarily varying these two parameters is shown in Figure 9. A grid of model solutions was generated with the eddy diffusion rates arbitrarily increased, and decreased, by a factor of two, and for the vertical advection increased, and decreased, by 0.2 cm s⁻¹. Reducing the eddy diffusion rate causes a decrease in the H₂O mixing ratio at 90 km, the result of the ongoing loss of water vapour by Lyman α photodissociation, and also decreases the O₃ density with less O being mixed downwards. Increasing the vertical advection increases the H₂O mixing ratio at 90 km by moving H₂O rich air upwards and decreases O₃ by moving O deficient air upwards. The measured H₂O mixing ratio and O₃ density are

indicated by the large square in Figure 9. The width of the square is defined by the estimated H₂O measurement precision over the equatorial region and the height by that for O₃.

The baseline values for eddy diffusion and for vertical advection come close to simultaneously matching the measured H₂O mixing ratio and O₃ density. However, the model solution diverges rapidly when either of these two parameters is changed. Based on the estimated measurement precision it would appear that using the approach described here the vertical advection can be determined to within 0.1 cm s⁻¹ and the eddy mixing rate to within 2x10⁵ cm² s⁻¹.

These simulations suggest that dynamical effects including vertical advection and eddy diffusion are implicitly involved in the generation of the MSAO. Exactly how they are related to gravity wave momentum as discussed by Dunkerton [1982] three decades ago remains to be addressed.

Conclusions

Observational data from a number of sources has been assembled to investigate the equatorial MSAO with the aid of a 1D photochemical model that includes diurnal tides, vertical advection and eddy diffusion. The diurnal tides included in the simulation have been verified by comparison with a number of observed tidal signatures, in particular O, H₂O and CO diurnal variations. The two key measured parameters are the H₂O mixing ratio and the O₃ density. From the ACE-FTS observations the H₂O mixing ratio at 90 km in the equatorial region is observed to increase by a factor of approximately five from April to August. From the GOMOS observations the O₃ density at 90 km at the equator is found to decrease by approximately a factor of three from April to August.

The 1D model is used to investigate the impact of these observed seasonal variations. The analysis suggests that by constraining the model with the measured input parameters, namely the H₂O mixing ratio and the O₃ density, it is possible to derive unique values for the vertical advection rate and the eddy diffusion rate. For August, at the equator and 90 km altitude, an eddy diffusion rate of approximately 1x10⁶ cm² s⁻¹ and vertical advection of approximately 0.8 cm s⁻¹ are inferred. For April the corresponding values are approximately 4x10⁵ cm² s⁻¹ and 0.1 cm s⁻¹. Even though the 1D model solution here is limited in scope, the uncertainty in the derived eddy diffusion rates is estimated to be less than 2x10⁵ cm² s⁻¹ and in vertical advection to be less than 0.1 cm s⁻¹. Assuming this approach to inferring mesopause dynamics withstands further testing, the technique will markedly improve the measurement accuracy of vertical advection and eddy diffusion.

As a further check of the model results the simulated OH* 9-4 band emission, using model H and O₃ densities, was compared with the seasonal variation of the OH* 9-4 band observed by OSIRIS. Agreement in the trend in the seasonal variation was satisfactory while agreement in absolute brightness was poor.

It is apparent that the analysis presented here should be extended to latitudes outside the equatorial region to yield further insights into vertical advection and eddy diffusion. The process would benefit considerably if in future missions all the relevant parameters were measured simultaneously.

Acknowledgements

The Atmospheric Chemistry Experiment (ACE), also known as SCISAT-1, is a Canadian-led mission mainly supported by the Canadian Space Agency and the Natural Sciences and Engineering Research Council of Canada. Odin is a Swedish-led satellite project funded jointly by Sweden (SNSB), Canada (CSA), France (CNES) and Finland (Tekes). GOMOS on board ENVISAT is funded through the European Space Agency. The work of E. Kyrölä was supported by the Academy of Finland through the project MIDAT (#134325).

References

Adler-Golden, S. (1997), Kinetic parameters for OH nightglow modeling consistent with recent laboratory experiments, *J. Geophys. Res.*, **102**, 19969–19976, doi:10.1029/97JA01622.

Alexander, M. J., M. Geller, C. McLandress, S. Polavarapu, P. Preusse, F. Sassi, K. Sato, S. Eckermann, M. Ern, A. Hertzog, Y. Kawatani, M. Pulido, T.A. Shaw, M. Sigmond, R. Vincent, and S. Watanabe (2010), Recent developments in gravity-wave effects in climate models and the global distribution of gravity-wave momentum flux from observations and models. *Q.J.R. Meteorol. Soc.*, **136**, 1103–1124, doi: 10.1002/qj.637.

Bernath, P. F., McElroy, C. T., Abrams, M. C., Boone, C. D., Butler, M., Camy-Peyret, C., Carleer, M., Clerbaux, C., Coheur, P.-F., Colin, R., DeCola, P., De Mazière, M., Drummond, J. R., Dufour, D., Evans, W. F. J., Fast, H., Fussen, D., Gilbert, K., Jennings, D. E., Llewellyn, E.J., Lowe, R. P., Mahieu, E., McConnell, J. C., McHugh, M., McLeod, S. D., Michaud, R., Midwinter, C., Nassar, R., Wichita, F., Nolan, C., Rhineland, C. P., Rocha, Y. J., Rowland, N., Selenium, K., Simon, P., Skelton, R., Sloan, J. J., Saucy, M.-A., Strong, K., Tremblay, P., Turnbull, D., Walker, K. A., Walt, I., Wardle, D. A., Where, V., Sander, R., and Zoo, J. (2005), Atmospheric Chemistry Experiment (ACE): mission overview, *Geophys. Res. Lett.*, **32**, L15S01, doi:10.1029/2005GL022386.

Brasseur, G.P. and S. Solomon (2005), *Aeronomy of the Middle Atmosphere*, Springer, Dordrecht, The Netherlands.

Burrage, M.D., N. Arvin, W.R. Skinner, and P.B. Hays (1994), Observations of the O₂ atmospheric band nightglow by the High Resolution Doppler Imager, *J. Geophys. Res.*, **99**, 15,017-15,023.

Chabrillat, S. and G. Kockarts (1997), Simple parameterization of the solar Lyman-alpha line, *Geophys. Res. Lett.*, **24**, 2659-2662.

Chandra, S., C.H. Jackman, E.L. Fleming, and J.M. Russell III (1997), The seasonal and long term changes in mesospheric water vapor, *Geophys. Res. Lett.*, **24**, 639-642.

Cogger, L.L, R.D. Elphinstone, and J.S. Murphree (1981), Temporal and latitudinal 5577 Å airglow variations, *Can. J. Phys.*, **59**, 1296–1307.

Cosby, P.C. and T.G. Slanger (2007), OH spectroscopy and chemistry investigated with astronomical sky spectra, *Can. J. Phys.*, **85**, 77-99.

Dikty, S., H. Schmidt, M. Weber, C. von Savigny, and M.G. Mlynczak (2010), Daytime ozone and temperature variations in the mesosphere: a comparison between SABER observations and HAMMONIA model, *Atmos. Chem. Phys.*, **10**, 8331–8339.

Dunkerton, T.J. (1982), Theory of the mesopause semiannual oscillation, *J. Atmos. Sci.*, **39**, 2682-2690.

Fauliot, V, G. Thuillier, and F. Vial (1997), Mean vertical wind in the mesosphere-lower thermosphere region, (80-120 km) deduced from the WINDII observations on board UARS, *Ann. Geophys.* **15**, 1221-1231.

Fukuyama, K. (1977), Airglow variations and dynamics in the lower thermosphere and upper mesosphere- II. Seasonal and long-term variations, *J. Atmos. Terr. Phys.*, **39**, 1-14.

Hagan, M.E., M.D. Burrage, J.M. Forbes, J. Hackney, W.J. Randel, and X. Zhang, (1999), GSWM-98: results for migrating solar tides, *J. Geophys. Res.*, **104**, 6813–6827.

Hall, C.M., U.-P. Hoppe, T.A. Blix, E.V. Thrane, A.H. Manson, and C.E. Meek (1999), Seasonal variation of turbulent energy dissipation rates in the polar mesosphere: a comparison of methods, *Earth Planets Space*, **51**, 515–524.

Holton, J.R. (2004), An introduction to dynamic meteorology, Fourth edition, Elsevier.

Huang, F.T., H.G. Mayr, J.M. Russell III, M.G. Mlynczak, and C.A. Reber (2008), Ozone diurnal variations and mean profiles in the mesosphere, lower thermosphere, and stratosphere, based on measurements from SABER on TIMED, *J. Geophys Res.*, **113**, A04307, doi:10.1029/2007JA012739.

John, S.R. and K.K. Kumar (2011), TIMED/SABER observations of global cold point mesopause variability at diurnal and planetary wave scales, *J. Geophys Res.*, **116**, A06314, doi:10.1029/2010JA015945.

Kockarts, G (1994), Penetration of solar radiation in the Schumann-Runge bands of molecular oxygen: a robust approximation, *Ann. Geophys.*, **12**, 1207-1217.

Kyrölä, E., J. Tamminen, G.L. Leppelmeier, V. Sofieva, S. Hassinen, A. Seppala, P.T. Verronen, J.L. Bertaux, A. Hauchecorne, F. Dalaudier, D. Fussen, F. Vanhellemont, O. Fanton d'Andon, G. Barrot, A. Mangin, B.

Theodore, M. Guirlet, R. Koopman, L. Saavedra de Miguel, P. Snoeij, T. Fehr, Y. Meijer, and R. Fraisse (2006), Nighttime ozone profiles in the stratosphere and mesosphere by the Global Ozone Monitoring by Occultation of Stars on Envisat, *J. Geophys Res.*, **111**, D24306, doi:10.1029/2006JD007193.

Kyrölä, E., J. Tamminen, V. Sofieva, J. L. Bertaux, A. Hauchecorne, F. Dalaudier, D. Fussen, F. Vanhellefont, O. Fanton d'Andon, G. Barrot, M. Guirlet, T. Fehr, and L. Saavedra de Miguel (2010), GOMOS O₃, NO₂, and NO₃ observations in 2002–2008, *Atmos. Chem. Phys.*, **10**, 7723–7738.

Lewis, B.R., I.M. Vardavas and J.H. Carver (1983), The aeronomic dissociation of water vapour by solar Lyman α radiation, *J. Geophys. Res.*, **88**, 4935-4940.

Llewellyn, E.J., N.D. Lloyd, D.A. Degenstein, R.L. Gattinger, S.V. Petelina, A.E. Bourassa, J.T. Wiensz, E.V. Ivanov, I.C. McDade, B.H. Solheim, J.C. McConnell, C.S. Haley, C. von Savigny, C.E. Sioris, C.A. McLinden, E. Griffioen, J. Kaminski, W.F.J. Evans, E. Puckrin, K. Strong, V. Wehrle, R.H. Hum, D.J.W. Kendall, J. Matsushita, D.P. Murtagh, S. Brohede, J. Stegman, G. Witt, G. Barnes, W.F. Payne, L. Piché, K. Smith, G. Warshaw, D.-L. Deslauniers, P. Marchand, E.H. Richardson, R.A. King, I. Wevers, W. McCreath, E. Kyrölä, L. Oikarinen, G.W. Leppelmeier, H. Auvinen, G. Mégie, A. Hauchecorne, F. Lefèvre, J. de La Nöe, P. Ricaud, U. Frisk, F. Sjöberg, F. von Schéele and L. Nordh (2004), The OSIRIS Instrument on the Odin Spacecraft, *Can. J. Phys.*, **82**, 411-422.

Liu, A. Z. (2009), Estimate eddy diffusion coefficients from gravity wave vertical momentum and heat fluxes, *Geophys. Res. Lett.*, **36**, L08806, doi:10.1029/2009GL037495.

Lossow, S., J. Urban, J. Gumbel, P. Eriksson, and D. Murtagh (2008), Observations of the mesospheric semi-annual oscillation (MSAO) in water vapour by Odin/SMR, *Atmos. Chem. Phys.*, **8**, 6527–6540.

Marsh, D., A. Smith, and E. Noble (2003), Mesospheric ozone response to changes in water vapor, *J. Geophys. Res.*, **108**, 4109, doi:10.1029/2002JD002705.

McCormack, J.P., K. W. Hoppel, and D. E. Siskind (2008), Parameterization of middle atmospheric water vapor photochemistry for high-altitude NWP and data assimilation, *Atmos. Chem. Phys.*, **8**, 7519–7532.

McDade, I.C., D.P. Murtagh, R.G.H. Greer, P.H.G. Dickinson, G. Witt, J. Stegman, E.J. Llewellyn, L. Thomas, and D.B. Jenkins (1986), ETON 2: Quenching parameters for the proposed precursors of O₂(b¹Σ_g⁺) and O(¹S) in the terrestrial nightglow, *Planet. Space Sci.*, **34**, 789-800.

Murtagh, D., *et al.* (2002), An overview of the Odin atmospheric mission, *Can J. Phys.*, **80**, 309-319.

Picone, J.M., A.E. Hedin, D.P. Drob, and A.C. Aikin (2002), NRL-MSISE-00 Empirical Model of the Atmosphere: Statistical Comparisons and Scientific Issues, *J. Geophys. Res.*, **107**, 1468, doi:10.1029/2002JA009430.

- Portnyagin, Yu.I., T.V. Solov'eva, E.G. Merzlyakov, A.I. Pogorel'tsev, and E.N. Savenkova (2010), Height–Latitude Structure of the Vertical Wind in the Upper Mesosphere and Lower Thermosphere (70–110 km), *J. Atmos. Oceanic Phys.*, **46**, 85-94, DOI: 10.1134/S0001433810010123.
- Qian, L., S.C. Solomon, and T.J. Kane (2009), Seasonal variation of thermospheric density and composition, *J. Geophys. Res.*, **114**, A01312, doi:10.1029/2008JA013643.
- Richter, J.H. and R.R. Garcia (2006), On the forcing of the Mesospheric Semi-Annual Oscillation in the Whole Atmosphere Community Climate Model, *Geophys. Res. Lett.*, **33**, L01806, doi:10.1029/2005GL024378.
- Richter, J. H., F. Sassi, R. R. Garcia, K. Matthes, and C. A. Fischer (2008), Dynamics of the middle atmosphere as simulated by the Whole Atmosphere Community Climate Model, version 3 (WACCM3), *J. Geophys. Res.*, **113**, D08101, doi:10.1029/2007JD009269.
- Russell, J.P., W.E. Ward, R.P. Lowe, R.G. Roble, G.G. Shepherd and B. Solheim (2005), Atomic oxygen profiles (80 to 115 km) derived from WINDII Imaging Interferometer/Upper Atmosphere Research Satellite measurements of the hydroxyl and greenline airglow: Local time-latitude dependence, *J. Geophys. Res.*, **110**, D15306, doi:10.1029/2004JD005570.
- Sander, S.P., R.R. Friedl, J.P.D. Abbatt, J.R. Barker, J.B. Burkholder, D.M. Golden, C.E. Kolb, M.J. Kurylo, G.K. Moortgat, P.H. Wine, R.E. Huie, and V.L. Orkin (2011), Chemical Kinetics and Photochemical Data for Use in Atmospheric Studies, JPL Publication 10-6, Evaluation Number 17.
- Sasi, M.N. and L. Vijayan (2001), Turbulence characteristics in the tropical mesosphere as obtained by MST radar at Gadanki (13.5° N, 79.2° E), *Annals. Geophys.*, **19**, 1019–1025.
- Shapiro, A.V., E. Rozanov, A.I. Shapiro, S. Wang, T. Egorova, W. Schmutz, and Th. Peter (2012), Signature of the 27-day solar rotation cycle in mesospheric OH and H₂O observed by the Aura Microwave Limb Sounder, *Atmos. Chem. Phys.*, **12**, 3181–3188, doi:10.5194/acp-12-3181-2012.
- Sharp, W.E. and D. Kita (1987), In Situ Measurement of Atomic Hydrogen in the Upper Mesosphere, *J. Geophys. Res.*, **92**, 4319-4324.
- Sheese, P.E., I.C. McDade, R.L. Gattinger, and E.J. Llewellyn (2011), Atomic oxygen densities retrieved from Optical Spectrograph and Infrared Imaging System observations of O₂ A-band airglow emission in the mesosphere and lower thermosphere, *J. Geophys. Res.*, **116**, D01303, doi:10.1029/2010JD01464.

- Shepherd, M.G., Guiping Liu, and G. G. Shepherd (2006), Mesospheric semiannual oscillation in temperature and nightglow emission, *J. Atmos. Solar Terr. Phys.*, **68** 379–389.
- Skinner, W.R., J.H. Yee, P.B. Hays, and M.D. Burrage (1998), Seasonal and local time variations in the O(¹S) green line, O₂ atmospheric band and OH Meinel band emissions as measured by the High Resolution Doppler Imager, *Adv. Space Res.*, **21**, 835–841.
- Smith, A.K. (2004), Physics and chemistry of the mesopause region, *J. Atmos. Solar Terr. Phys.*, **66**, 839–857.
- Smith, A.K. and D.R. Marsh (2005), Processes that account for the ozone maximum at the mesopause, *J. Geophys. Res.*, **110**, D23305, doi:10.1029/2005JD006298.
- Smith, A.K., D.R. Marsh, J.M. Russell III, M.G. Mlynczak, F.J. Martin-Torres, and Erkki Kyrölä (2008), Satellite observations of high nighttime ozone at the equatorial mesopause, **113**, D17312, doi:10.1029/2008JD010066.
- Smith, A.K., D.R. Marsh, M.G. Mlynczak, and J.C. Mast (2010), Temporal variations of atomic oxygen in the upper mesosphere from SABER, *J. Geophys. Res.*, **115**, D18309, doi:10.1029/2009JD013434.
- Sonnemann, G.R. and U. Körner (2003), Total hydrogen mixing ratio anomaly around the mesopause region, *J. Geophys. Res.*, **108**, doi:10.1029/2002JD003015.
- Thomas, R.J. (1990), Seasonal Ozone Variations in the Upper Mesosphere, *J. Geophys. Res.*, **95**, 7395-7401.
- Thomas, R.J. (1995), Atomic Hydrogen and Atomic Oxygen Density in the Mesopause Region: Global and Seasonal Variations Deduced From Solar Mesosphere Explorer Near-Infrared Emissions, *J. Geophys. Res.*, **95**, 16,457-16,476.
- Tian, F., J.F. Kasting, H-L. Liu, and R.G. Roble (2008), Hydrodynamic planetary thermosphere model: 1. Response of the Earth's thermosphere to extreme EUV conditions and the significance of adiabatic cooling, *J. Geophys. Res.*, **113**, E05008, doi:10.1029/2007JE002946.
- Van der Loo, M.P.J. and G.C. Groenenboom (2007), Theoretical transition probabilities for the OH Meinel system, *J. Chem. Phys.*, **126**, 114314-114317.
- Van der Loo, M.P.J. and G.C. Groenenboom (2008), Erratum: “Theoretical transition probabilities for the OH Meinel system” [*J. Chem. Phys.* **126**, 114314, 2007], *J. Chem. Phys.*, **128**, doi: 10.1063/1.2899016, 159901-2.

Wu, Q., D.A. Ortland, T.L. Killeen, R.G. Roble, M.E. Hagan, H.-L. Liu, S.C. Solomon, J. Xu, W.R. Skinner, and R.J. Niciejewski (2008), Global distribution and interannual variations of mesospheric and lower thermospheric neutral wind diurnal tide: 1. Migrating tide, *J. Geophys. Res.*, **113**, doi: 10.1029/2007JA012542.

Xu, J., H. Gao, A.K. Smith, and Y. Zhu (2012), Using TIMED/SABER nightglow observations to investigate hydroxyl emission mechanisms in the mesopause region, *J. Geophys. Res.*, **117**, D02301, doi:10.1029/2011JD016342.

Yee, J.-H., R.G. Roble, W.R. Skinner, M.D. Burrage, and P.B. Hays (1997), Global simulations and observations of O(¹S), O₂(¹Σ) and OH mesospheric nightglow emissions, *J. Geophys. Res.* **102**, 19,949-19,968.

Figure 1a – H₂O profiles for model days seven through eight for April equatorial conditions. The model initial conditions are from the ACE-FTS occultation measurements. The effect of the diurnal tide is apparent.

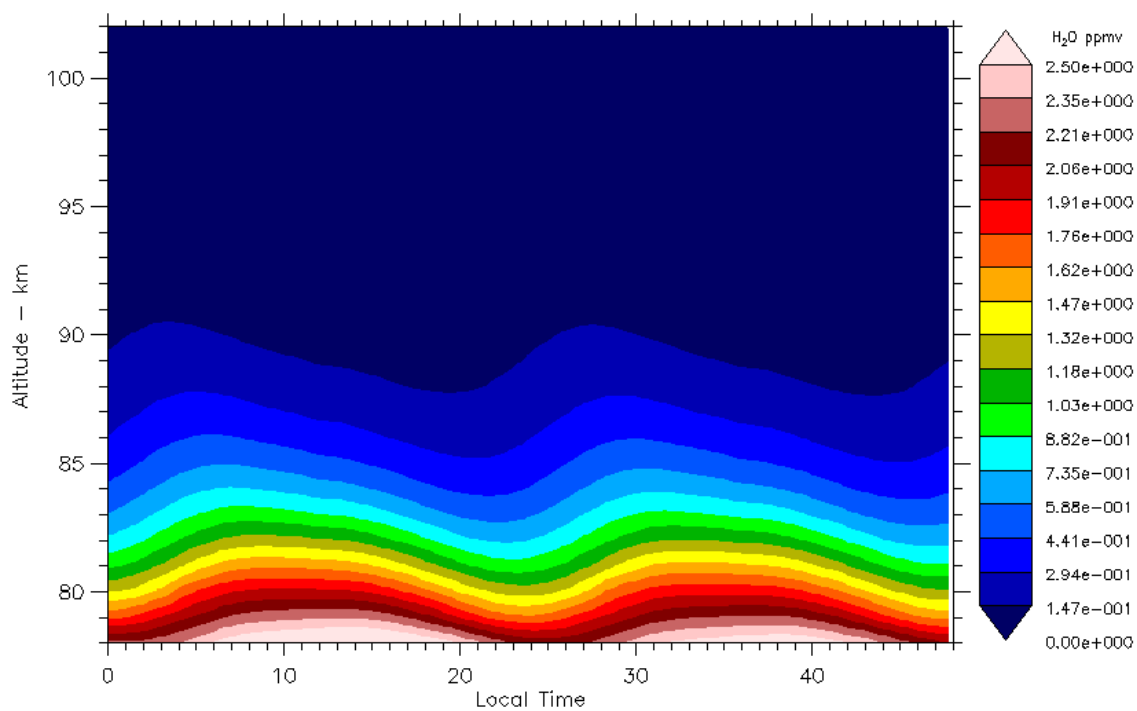


Figure 1b – H₂O profiles for model days seven through eight for August equatorial conditions. Note the scale is 1.32 times larger than in Figure 1a. The August 90 km H₂O mixing ratio is approximately five times larger than for April.

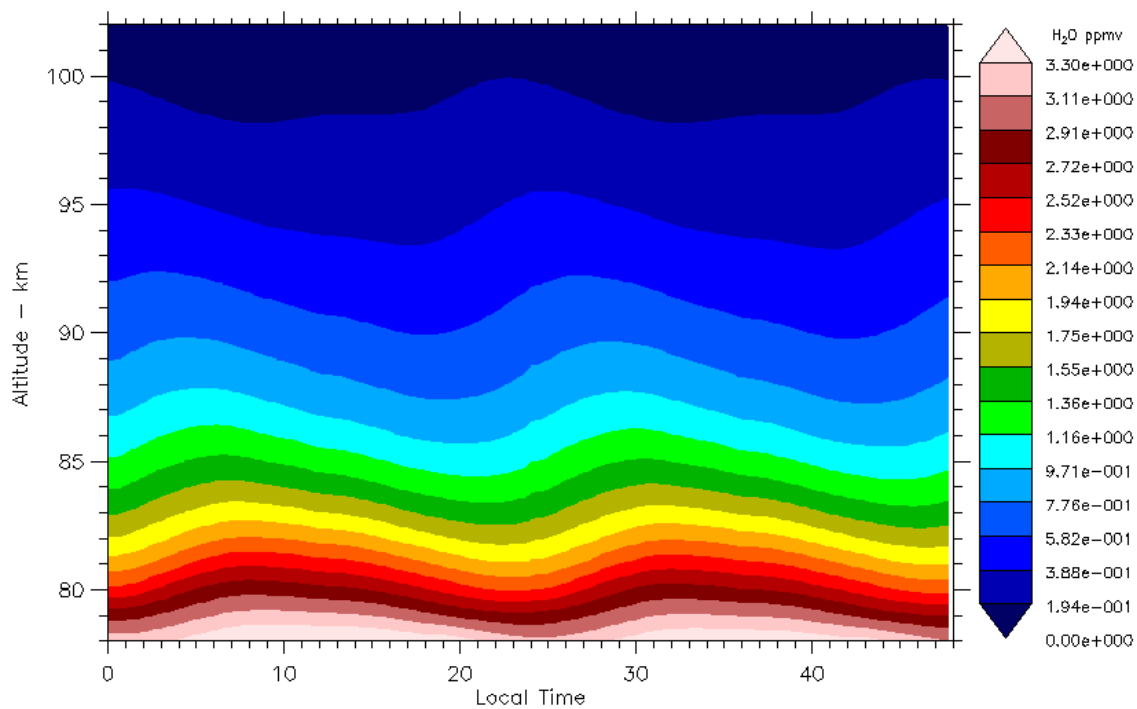


Figure 2a – Simulated H for model days seven through eight for April at the equator. The dominant determining factors are the H₂O mixing ratio, from the ACE-FTS measurements, and the Lyman α flux from the SORCE dataset.

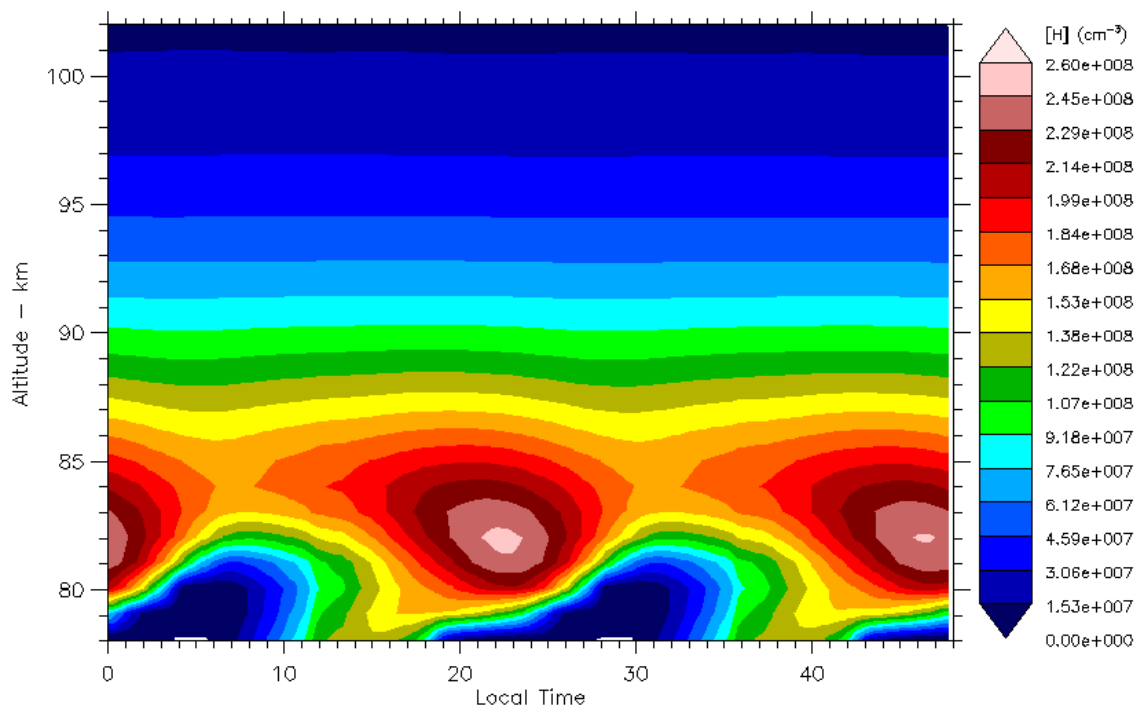


Figure 2b – Model H for model days seven through eight for August at the equator. Note the scale is 1.12 times larger than in Figure 2a. From 85 to 90 km the April H values are approximately two-thirds the August values.

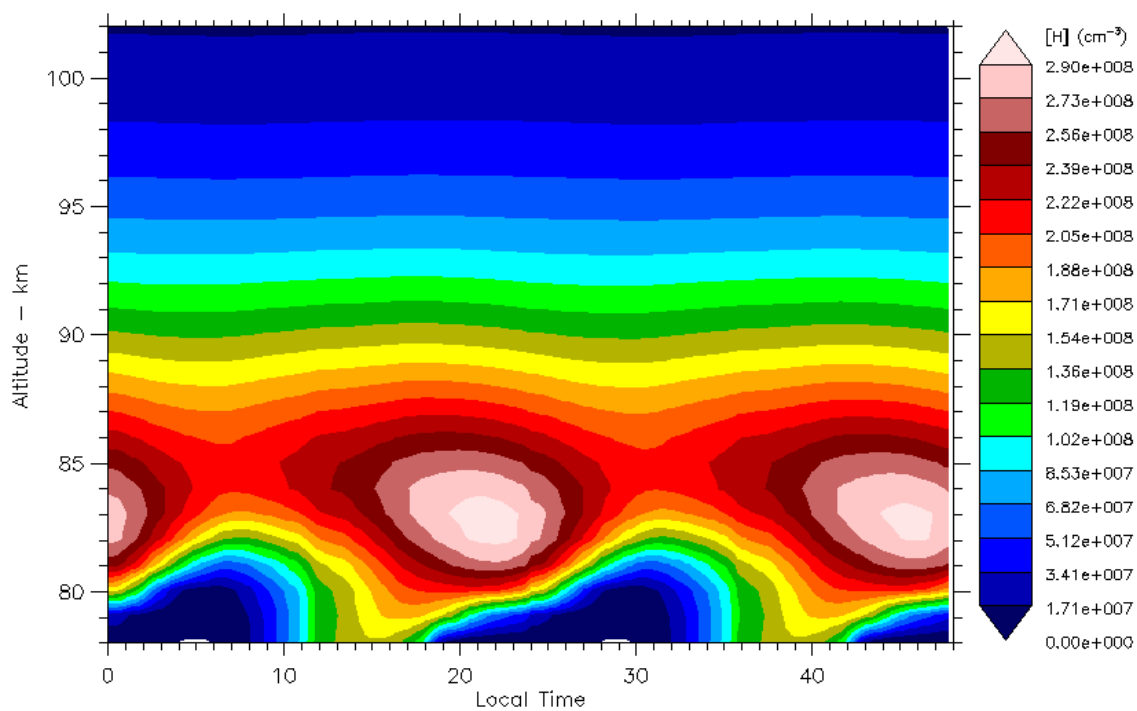


Figure 3a – Local time variation of O for model days seven through eight in the April equatorial region. The effects of the diurnal tides are evident. The tidal phases compare well with the SABER O observations by Smith *et al.* [2010] and Russell *et al.* [2005].

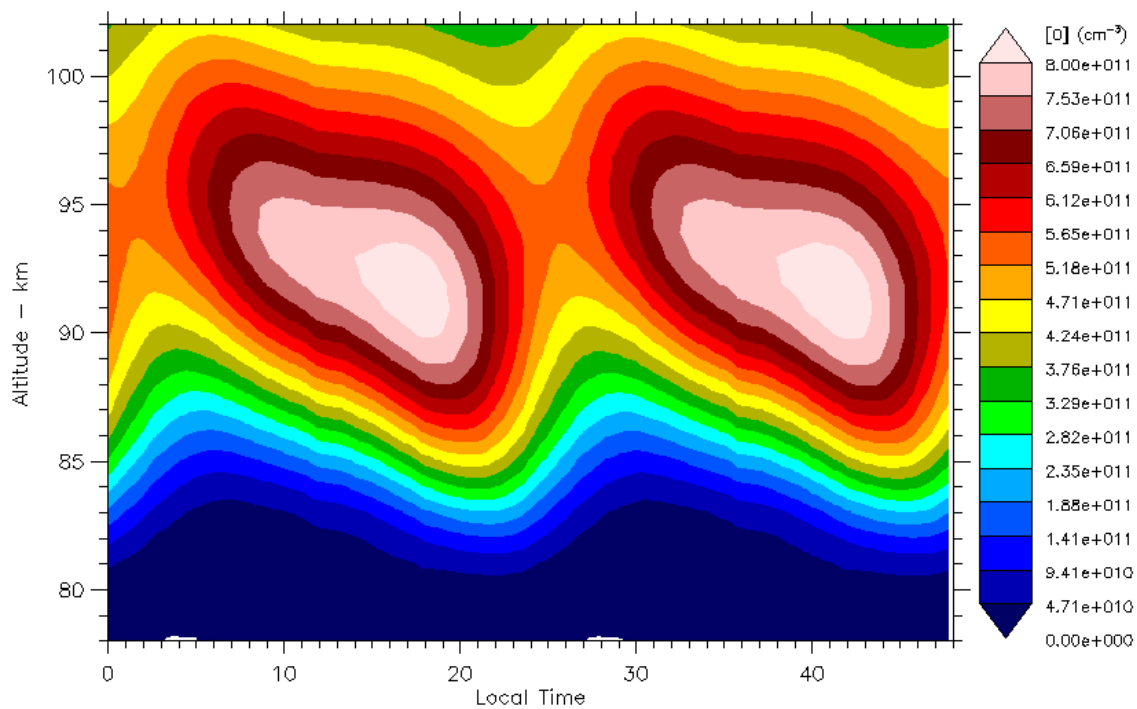


Figure 3b – Local time variation of O for model days seven through eight in the equatorial region for August. The effects of the diurnal tides are again evident. Note the scale is 2.28 times smaller than in Figure 3a. The maximum O densities are less than one-half those for April in Figure 3a.

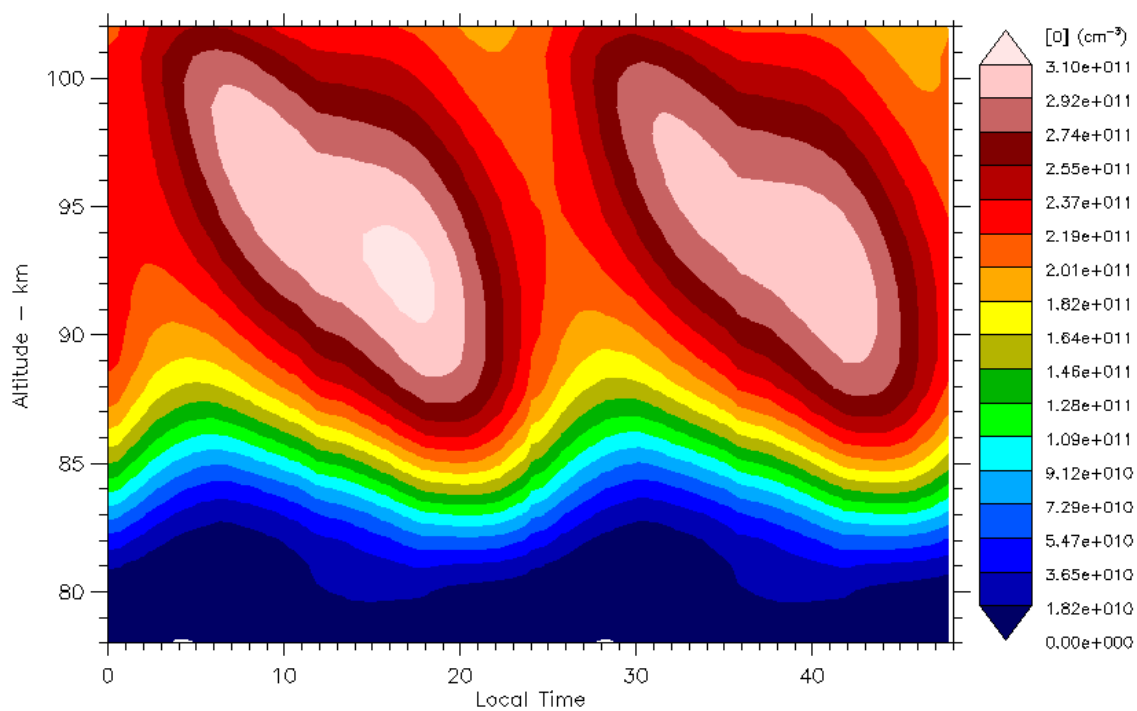


Figure 4a – Local time variation of O_3 for model days seven through eight in the equatorial region for April. The effects of the diurnal tides are again evident. The large increase in O_3 just before sunrise is co-located with the diurnal temperature minimum and indicates the change in the O and O_3 partitioning with temperature.

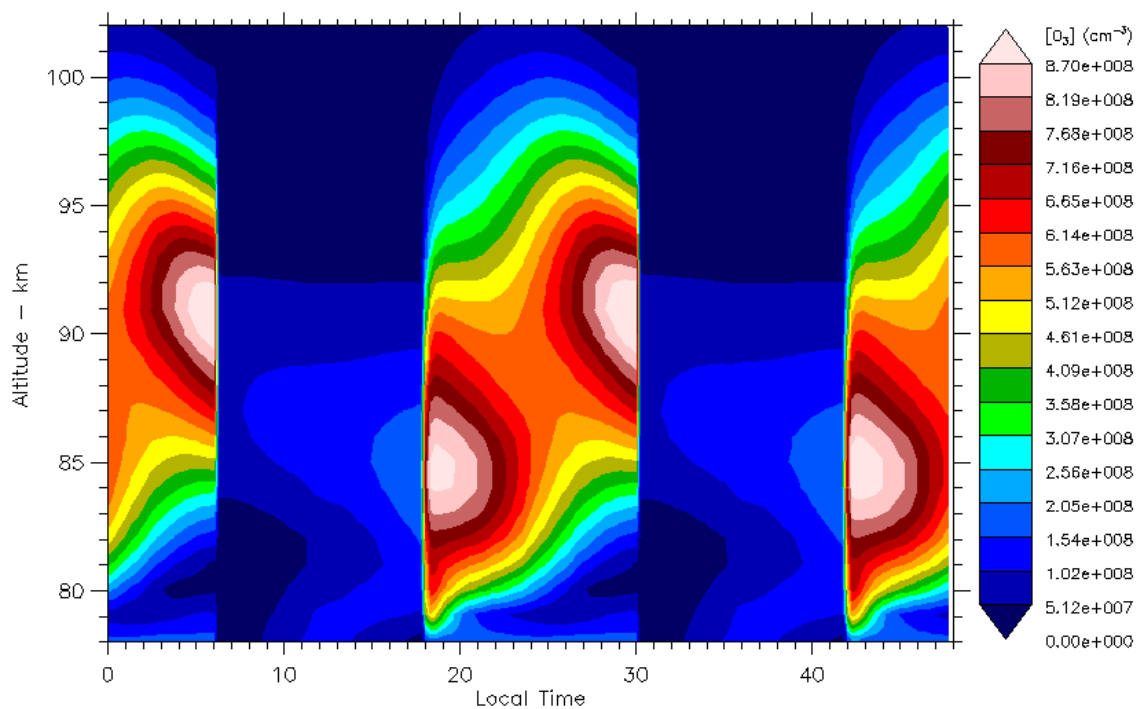


Figure 4b – Local time variation of O₃ for model days seven through eight in the equatorial region for August. The effects of the diurnal tides are again evident. Note the scale is 1.98 times smaller than in Figure 4a. The August O₃ densities are approximately one-third the April densities.

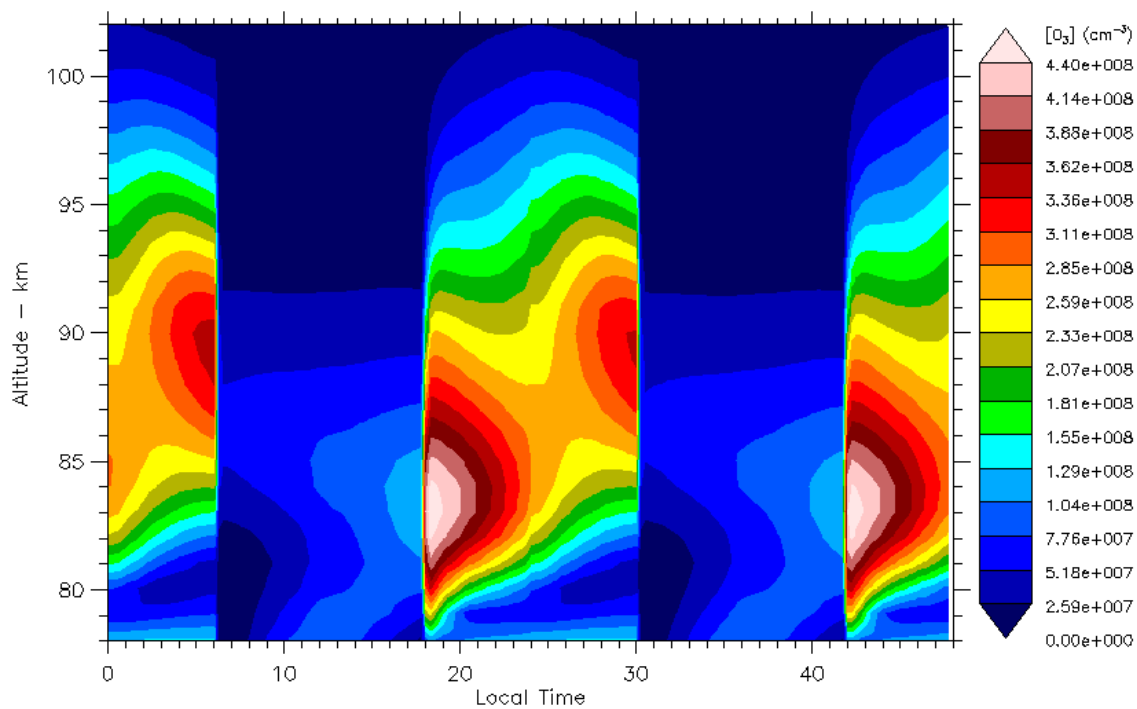


Figure 5a – ACE-FTS mixing ratio observations for April 2005 sunrise and sunset at the equator showing the effects of the diurnal tides on CO and H₂O. The tides are out of phase, as expected, since the changes in mixing ratio profiles with altitude are of opposite sign.

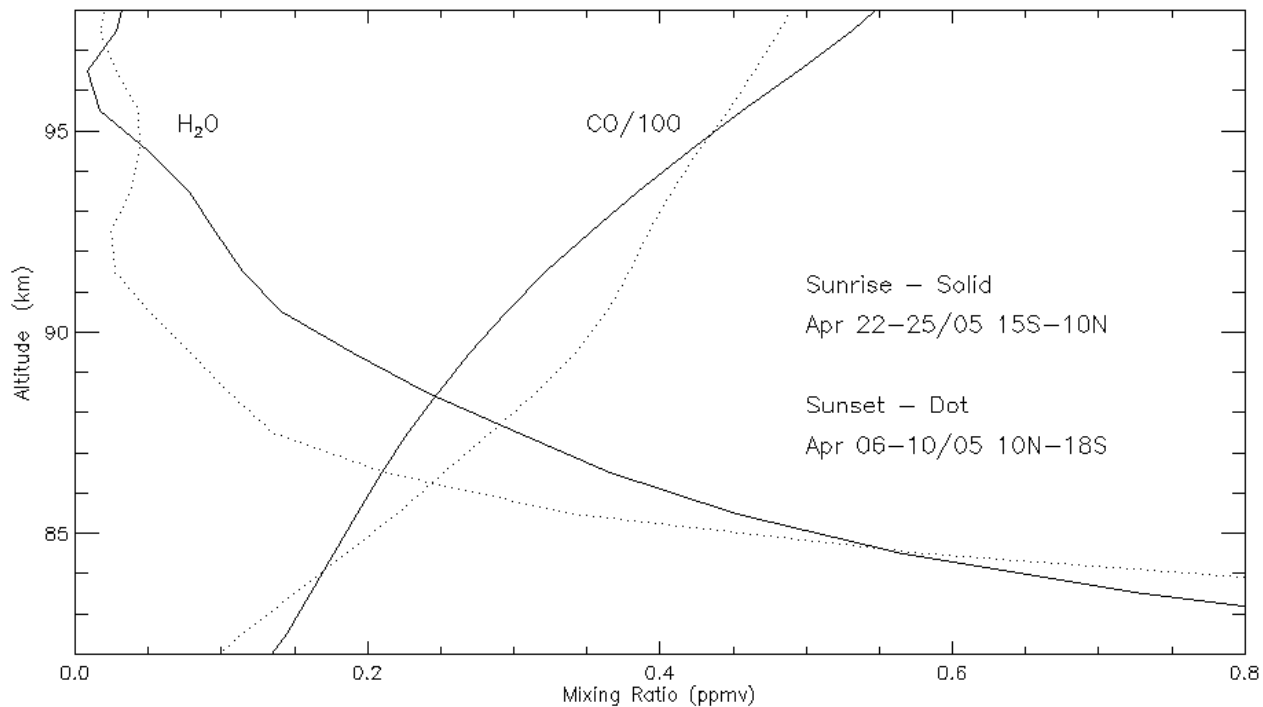


Figure 5b – Model diurnal tide for CO for April, days seven through eight, for comparison with the ACE-FTS sunrise/sunset observations. At 90 km altitude the sunrise mixing ratio is smaller than the sunset mixing ratio, as in Figure 5a.

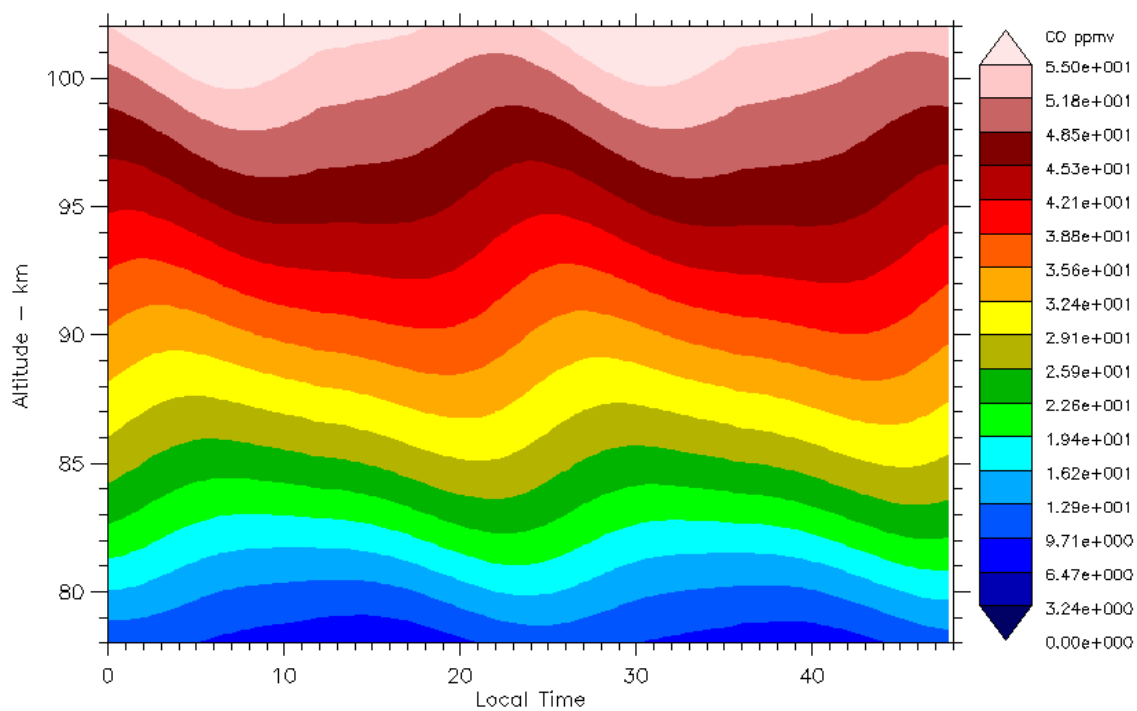


Figure 6 – The mesospheric semi-annual oscillation of O₃ density observed by the GOMOS instrument for night-time conditions is shown. Monthly averages are included where available for years from 2003 to 2008. The two large squares indicate the model O₃ densities for April “near equinox” and August “near solstice” conditions for approximately 23 H local time with baseline eddy diffusion and background vertical winds. Symbols for 2003 to 2008 respectively : plus sign, asterisk, period, diamond, triangle, and square.

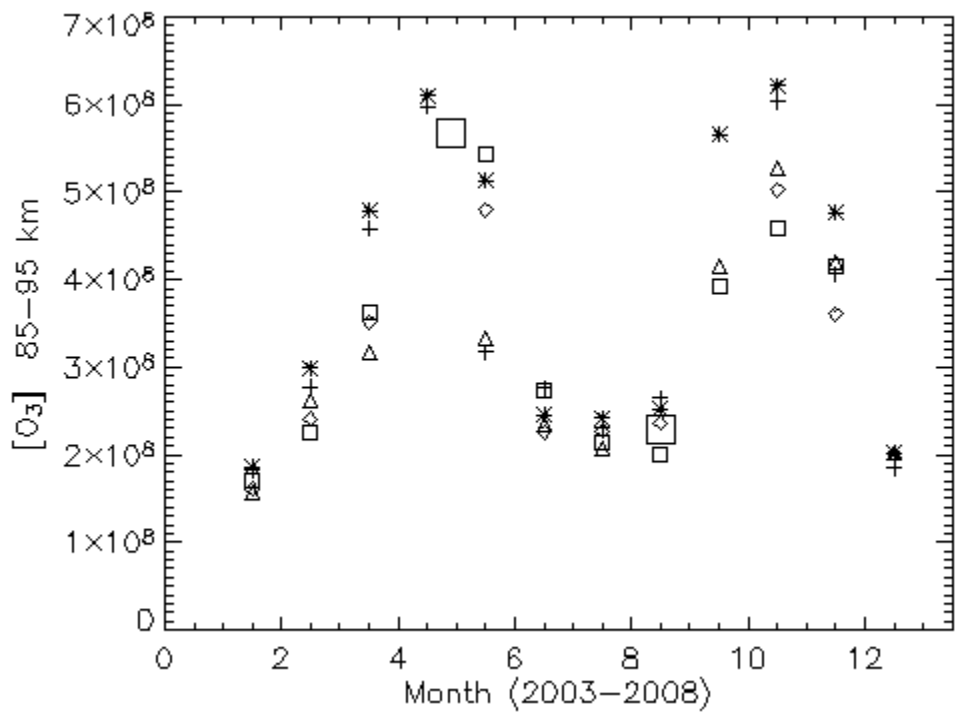


Figure 7a – Model OH* 9-4 volume emission rates for April, days seven through eight, from model [O₃] and [H] values. Rates are from Adler-Golden [1997]. VER units are in photons cm⁻³s⁻¹.

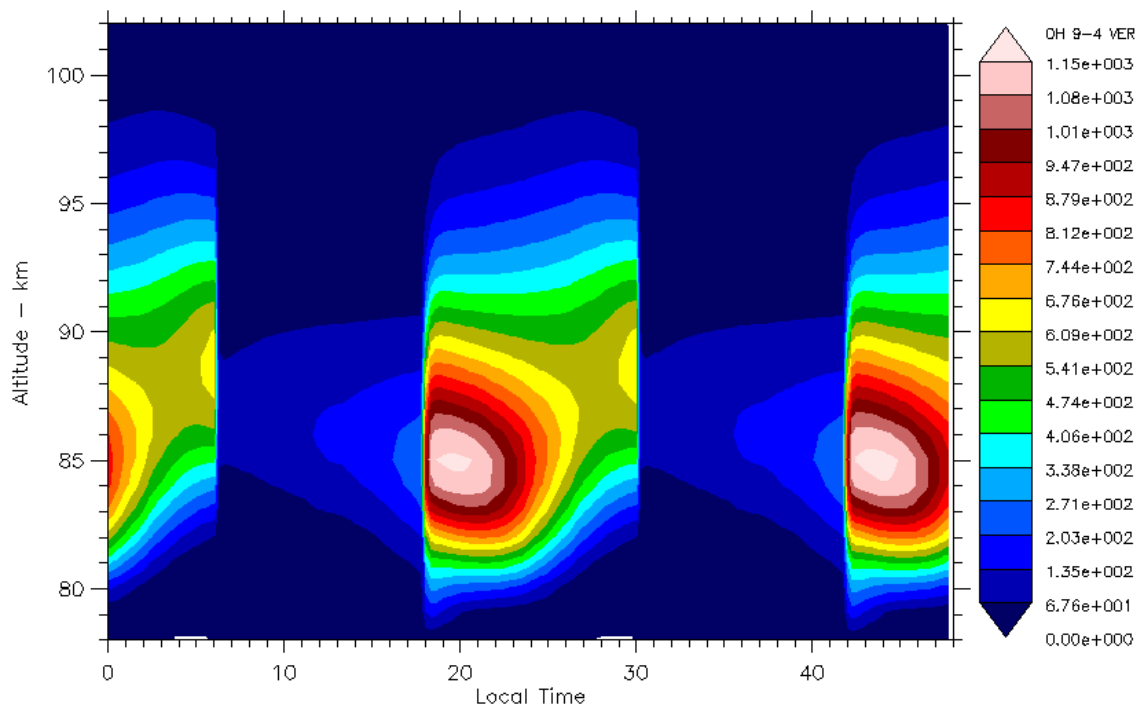


Figure 7b – Model OH* 9-4 volume emission rates for August, days seven through eight, from model [O₃] and [H] values. Note the scale is 1.77 times smaller than in Figure 7a. VER units are in photons cm⁻³s⁻¹.

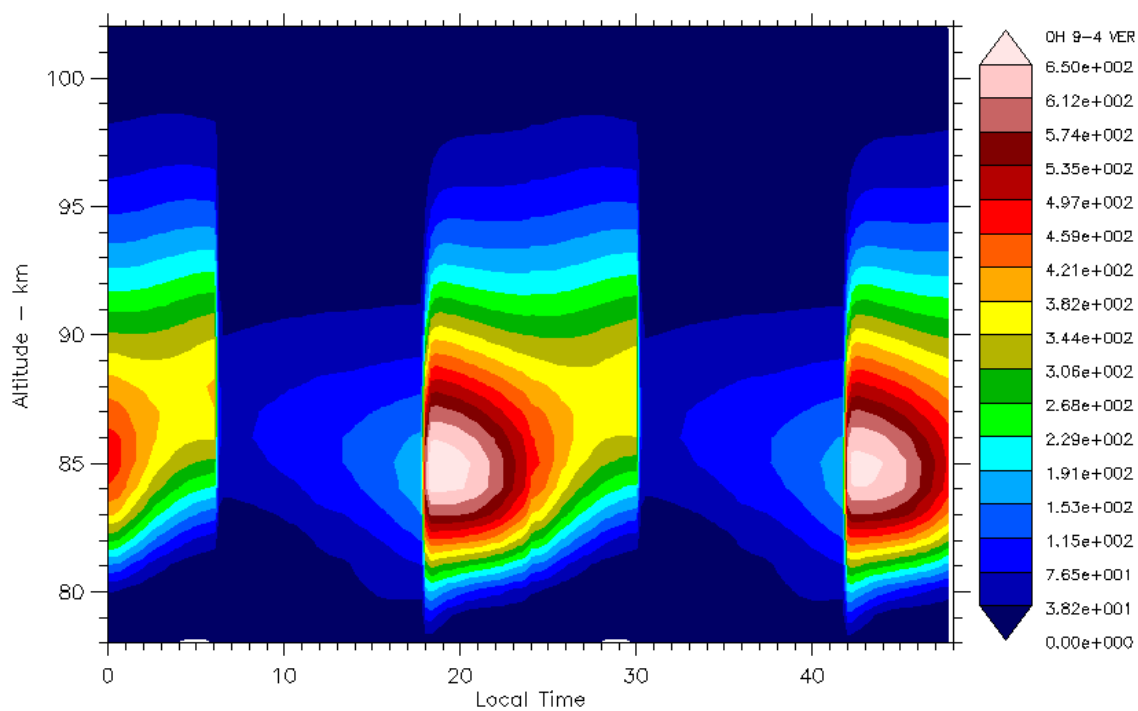


Figure 8 – Monthly averages of the OH* 9-4 brightness, referred to zenith viewing, as observed by OSIRIS in the equatorial region from 2004 to 2011 (plus signs). The April and August model OH* 9-4 brightness with rates from Adler-Golden [1997] are given by the square symbols. The diamond symbols are with the rate for OH* ($v'=9$) removal by O arbitrarily scaled up by 3, near gas kinetic.

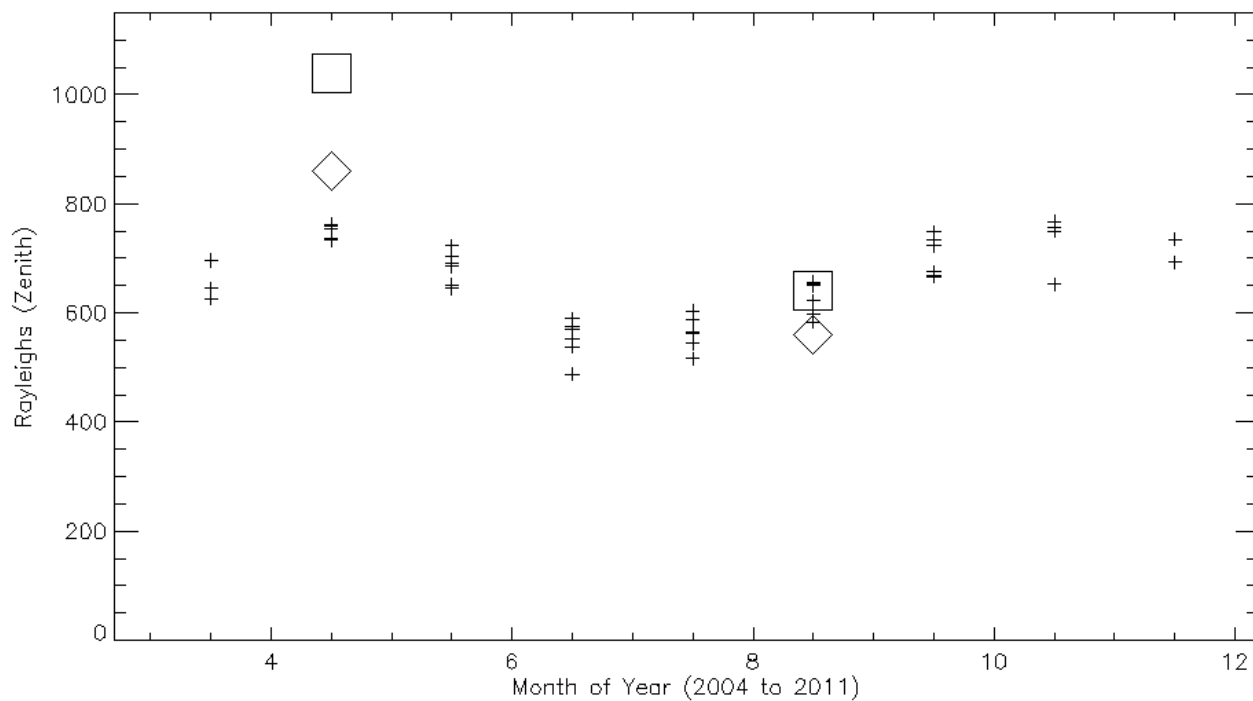


Figure 9 – The relationship between the combined effects of assumed eddy diffusion rates and vertical advection and the model O₃ density and H₂O mixing ratio at an altitude of 90 km in August. The large square locates the H₂O mixing ratio measured by ACE-FTS and the O₃ density measured by GOMOS (see text) The plus signs are for an assumed vertical advection of 0.6 cm s⁻¹, the asterisks for 0.8 cm s⁻¹ and the triangles for 1.0 cm s⁻¹. The dotted line is for an assumed eddy diffusion rate of approximately 5x10⁵ cm² s⁻¹, the dashed line for 1.0x10⁶ cm² s⁻¹ and the dot-dash line for 2x10⁶ cm² s⁻¹.

